Journal of Materials Chemistry A

ROYAL SOCIETY OF CHEMISTRY

COMMUNICATION

View Article Online
View Journal | View Issue

Check for updates

Cite this: J. Mater. Chem. A, 2024, 12, 7528

Received 5th January 2024
Accepted 5th March 2024

DOI: 10.1039/d4ta00091a

rsc.li/materials-a

Published on 06 mars 2024. Downloaded on 2.6.2026 13:51:06.

Modulation of the electronic structure of metallic bismuth catalysts by cerium doping to facilitate electrocatalytic CO_2 reduction to formate†

Yangyuan Zhang,‡[a] Shilong Liu,‡[a] Nannan Ji,[a] Lingzhi Wei,[a] Qiyang Liang,[a] Jiejie Li,[b] Ziqi Tian,*[b] Jianwei Su*[a] and Qianwang Chen*[c]

Metallic bismuth (Bi) can maintain a stable structure at high reduction potential during the CO_2 reduction reaction (CO_2RR) process; however, it is limited by its relatively unfavorable catalytic activity. To address this limitation, an effective strategy of electronic structure modulation can be employed to optimize the adsorption energy of reaction intermediates for enhancing CO_2RR performance. Based on this principle, we have developed a highly efficient and stable electrocatalyst comprising metallic Ce-doped Bi(0) nanoparticles encapsulated in a porous carbon framework. This catalyst exhibits a substantial improvement in CO_2RR activity compared with its undoped counterpart, driving a current density of 13.7 mA cm^{-2} with a faradaic efficiency of 97.2% for formate production at −1.1 V *versus* the reversible hydrogen electrode. Furthermore, long-term stability was achieved with an average faradaic efficiency close to 94% during a 48 hour electrocatalytic test. Density functional theory calculations, combined with the *in situ* attenuated total reflectance infrared (ATR-IR) spectroscopic study, indicate that the doping of Ce enriches the electron density around Bi, consequently enhancing the binding energy between the Bi active centers and *OCHO intermediates, thereby lowering the energy barrier for the CO_2RR to formic acid.

Electrochemical energy conversion systems provide the ability to store renewable energy as chemical energy, which helps overcome the geographical and seasonal limitations associated with these energy sources.[1] In this regard, the carbon dioxide reduction reaction (CO_2RR) technology is considered as a promising strategy to address energy challenges by converting the greenhouse gas CO_2 into value-added hydrocarbon products, additionally offering a potential solution for mitigating environmental issues.[2] In general, multiple competing reactions are simultaneously involved in the progression of the CO_2RR, yielding a wide variety of potential products, including hydrogen, carbon monoxide, formate, methanol, methane, ethylene and so on.[3–7] Among them, formic acid (HCOOH) and formate salts ($HCOO^-$) stand out as liquid-phase products with high energy density, facilitating convenient storage and transportation. Additionally, formic acid can serve as a hydrogen carrier for fuel cells and finds numerous applications in medicine.[8] Despite its significant role in environmental protection and the sustainable energy cycle, the CO_2RR process is hindered by the impractically high overpotential needed to surpass the initial energy barrier involved in the formation of the CO_2^- intermediate.[9–12] Therefore, highly efficient electrocatalysts are still in high demand to satisfy the requirements of catalytic activity and formate selectivity.

To date, extensive research has been conducted to develop efficient electrocatalysts for the high-selectivity and high-activity production of formate, primarily focusing on metal-based materials, including Hg, Pb, In, Sn, Bi and so on.[13–21] Specifically, Bi-based materials have gained significant attention as a prominent research area and made some progress due to their cost-effectiveness, abundance in the earth, non-toxicity, and superior catalytic activity.[22–25] Significantly, current research tends to focus on the Bi(III) species contained in various Bi-based compounds, such as oxides, sulfides, and composites.[22,23,25] However, the CO_2RR is a cathodic electrolysis process at high reduction potential, where Bi(III) species are prone to reduction during electrocatalysis.[24,26–28] This susceptibility leads to a reductive reconstruction at the electrocatalyst's surface, complicating the evaluation of the catalytic mechanism. Moreover, such a reconstruction may result in unintended variations in the active site configuration and CO_2RR performance, potentially contributing to the inferior stability of Bi(III)-based catalysts.[29,30] Thus, an efficient approach to

[a]Institutes of Physical Science and Information Technology, Key Laboratory of Structure and Functional Regulation of Hybrid Materials, Anhui University, Hefei 230601, China. E-mail: sujianwei@ahu.edu.cn

[b]Key Laboratory of Advanced Fuel Cells and Electrolyzers Technology of Zhejiang Province, Ningbo Institute of Materials Technology and Engineering, Chinese Academy of Sciences, Ningbo 315201, China. E-mail: tianziqi@nimte.ac.cn

[c]Hefei National Laboratory for Physical Science at Microscale, Department of Materials Science & Engineering, University of Science and Technology of China, Hefei 230026, China. E-mail: cqw@ustc.edu.cn

† Electronic supplementary information (ESI) available. See DOI: https://doi.org/10.1039/d4ta00091a

‡ These authors contributed equally to this work.

This journal is © The Royal Society of Chemistry 2024

Published on 06 mars 2024. Downloaded on 2.6.2026 13:51:06.

circumvent this reduction involves the direct employment of metallic Bi(0) as the active site in Bi-based materials, offering enhanced durability for cathodic CO_2RR applications.

However, the activity of formate production for Bi(0)-based catalysts is still not satisfactory for practical application in the CO_2RR, necessitating further improvement.[31,32] In essence, the CO_2RR activity and selectivity of the generation of formate are greatly constrained by the substantial energy barriers, which are closely associated with the weak binding energetics of *OCHO intermediates at Bi sites.[33,34] It is a consensus that heteroatom incorporation is a general strategy to modulate the intrinsic electronic structure of catalysts.[35,36] The electronic density of states of Bi p-orbitals can be efficiently modified after the appropriate introduction of heteroatoms, consequently increasing the adsorption of *OCHO intermediates and, in turn, boosting the intrinsic activity of Bi sites.[37,38] Rare earth elements are commonly considered "vitamins" of the modern industry due to their widespread use as dopants for material modulation.[39,40] Despite their potential, doping with rare earth elements has not been extensively explored in Bi(0)-based materials. Specifically, cerium (Ce) stands out among these rare earth elements due to its abundant availability and remarkable ability to regulate the electronic structure.[41,42] These characteristics make Ce an excellent candidate for doping into Bi-based catalysts. Therefore, Bi(0)-based materials by integration with Ce are postulated to significantly improve the CO_2RR catalytic performance for formate production.

Building upon this concept, we synthesized a catalyst consisting of Ce-doped Bi(0) nanoparticles encapsulated in a porous carbon framework by directly annealing a Ce-exchanged Bi-BTC precursor in an Ar atmosphere. Remarkably, the best-performing catalyst, containing a 4.09 wt% Ce content, exhibited a faradaic efficiency of 97.2% for formate production at −1.1 V *versus* the reversible hydrogen electrode (RHE) during the H-cell test, which can be compared to the highest faradaic efficiency of previously reported catalysts. Furthermore, the catalyst displayed long-term stability with an average faradaic efficiency close to 94% for formate production during the 48 hour chronoamperometry measurement. Density functional theory (DFT) calculations, combined with the *in situ* experimental data, confirmed the promoting influence of Ce doping into a metallic Bi catalyst for formic acid production through facilitating the adsorption of crucial *OCHO intermediates and adjusting the electronic structure.

Obviously, Scheme 1 depicts the synthetic route involved in preparing Ce-doped Bi encapsulated in porous carbon framework catalysts (details available in the Experimental section of the ESI†). In Scheme 1a, the Bi-BTC precursor was synthesized by using $Bi(NO_3)_2 \cdot 5H_2O$ and H_3BTC using a solvothermal method at 130 °C for 48 h. Afterward, Ce atoms were introduced into Bi-BTC by a simple ion–exchange reaction in the liquid phase (in Scheme 1b).[43] The Ce content in Ce-doped Bi-BTC precursors was controlled by the addition amount of $Ce(NO_3)_3$ solution, and the resulting products were hereinafter denoted as Ce_1Bi-BTC, Ce_2Bi-BTC and Ce_3Bi-BTC, respectively. As illustrated in the scanning electron microscopy (FESEM) images (Fig. S1†), the as-obtained Ce-exchanged Bi-BTC precursors all exhibit a uniform nanorod-like morphology similar to that of the original Bi-BTC precursor, consisting of layered stripe structures with a mean breadth of about 3 μm. X-ray diffraction (XRD) patterns reveal that the Ce-exchanged Bi-BTC precursors exhibit a high degree of crystallinity, consistent with the Bi-BTC MOF structure (in Fig. S2†).[31] Clearly, the introduction of Ce had no significant impact on the structural configuration of Bi-BTC. As shown in Scheme 1c, the Ce-doped Bi encapsulated in porous carbon framework catalysts was obtained by the annealing of precursors under an Ar atmosphere. The prepared products were hereinafter denoted as Bi@C, Ce_1–Bi@C, Ce_2–Bi@C, and Ce_3–Bi@C, where the corresponding Ce contents were 0 wt%, 1.15 wt%, 4.09 wt% and 6.02 wt%, respectively, according to the inductively coupled plasma atomic emission spectrometry (ICP-AES) results (in Table S1†). In Scheme 1d, the Ce–Bi@C nanorods are assembled by numerous small nanoparticles, where the formation of Ce–Bi nanoparticles can prevent agglomeration by rapidly anchoring onto the outer carbon layers. Such a hierarchical structure is beneficial for the improvement of catalytic activity and durability.

As revealed in the SEM and transmission electron microscope (TEM) images in Fig. 1a–c and S3–S5,† all the resultant products basically inherited the nanorod-like morphology, with a slightly smaller diameter. Interestingly, the nanorods are composed of uniform small nanoparticles tightly clamped between layered carbon nano-stripes, which are beneficial for rapid mass transfer during electrocatalysis. Interestingly, Ce–Bi nanoparticles seem to be less likely to be encapsulated by a carbon matrix with higher Ce doping content (Fig. S5†). Furthermore, we subjected Bi@C and Ce_2–Bi@C to oxidation in an air atmosphere at 200 °C for 30 minutes as shown in Fig. S7.† Despite the low temperature, oxygen was able to easily oxidize the Bi(0) nanoparticles inside Ce_2–Bi@C completely, suggesting the negligible impedance of mass transfer for a porous carbon framework. However, some Bi(0) particles remained unoxidized within Bi@C, indicating that a small amount of Bi(0) particles is completely encapsulated and isolated by carbon layers. This may be because during annealing, carbon clusters dissolved in Bi, and upon cooling, graphite layers precipitated.[44,45] The introduction of Ce reduces the solubility of carbon in Bi, resulting in less carbon precipitation around Bi during cooling. The XRD patterns of the obtained catalysts are displayed in Fig. 2a. These catalysts demonstrate an orthorhombic crystal structure corresponding to metallic Bi (PDF #85-1331). However, the XRD peaks shift left towards smaller 2θ angles with the increment of Ce content, which can be seen upon a closer inspection of the magnified peak in Fig. 2b. Such a shift is attributed to the subtle lattice expansion in Bi caused by the incorporation of Ce, which possesses a larger atomic radius than Bi.[46] Hence, the XRD peak displacement can provide solid evidence for the successful doping of Ce into the Bi-based catalysts.

In Fig. 1a–c, the best-performing sample, Ce_2–Bi@C, also exhibits a nanorod-like morphology assembled from nanoparticles, where Ce-doped metallic Bi nanoparticles ~50 nm in size are dispersed between the carbon layers. In Fig. 1d and e, the high-resolution (HR) TEM analysis images distinctly exhibit

Published on 06 mars 2024. Downloaded on 2.6.2026 13:51:06.

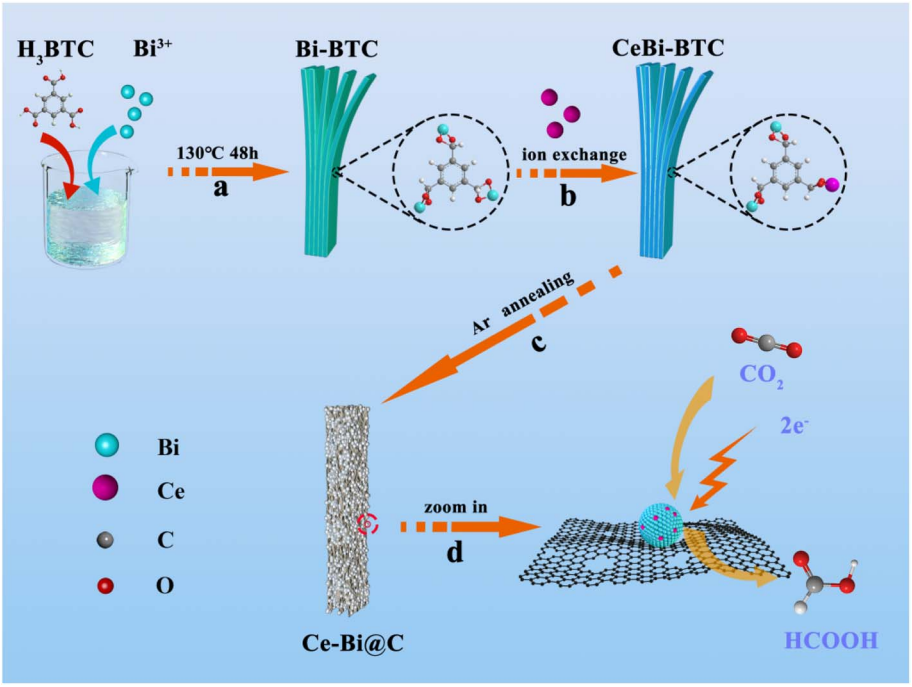

Scheme 1 Schematic illustration of the synthetic route and model of Ce–Bi@C.

lattice fringe spacings of 0.227, 0.237 and 0.329 nm, which correspond to the (110), (104) and (012) facets of the orthorhombic Bi phase. However, these lattice fringe spacings are slightly larger than the expected 0.226, 0.236 and 0.327 nm values for the standard Bi (110), (104) and (012) facets. Nevertheless, this discrepancy aligns well with the aforementioned XRD results, providing further confirmation of the successful incorporation of Ce into metallic Bi. From Fig. S6,† we confirm that the Ce–Bi nanoparticles are not entirely and tightly enveloped by carbon layers, which can expose the Bi active sites and facilitate rapid mass transfer throughout the porous carbon framework. As observed in energy dispersive X-ray spectroscopy (EDS) mapping images (Fig. 1f–i), Bi and Ce elements are uniformly distributed as small particles and surrounded by the C element, implying the formation of Ce-doped metallic Bi nanoparticles encapsulated in a porous carbon framework.

The chemical state and electronic structure of the catalysts were characterized using X-ray photoelectron spectroscopy (XPS) measurements. All XPS spectra were calibrated with the C 1s peak at 284.8 eV.[47,48] In Fig. S8,† the survey spectra of Ce–Bi@C catalysts demonstrate the additional presence of Ce compared with Bi@C. This result once again confirms that Ce

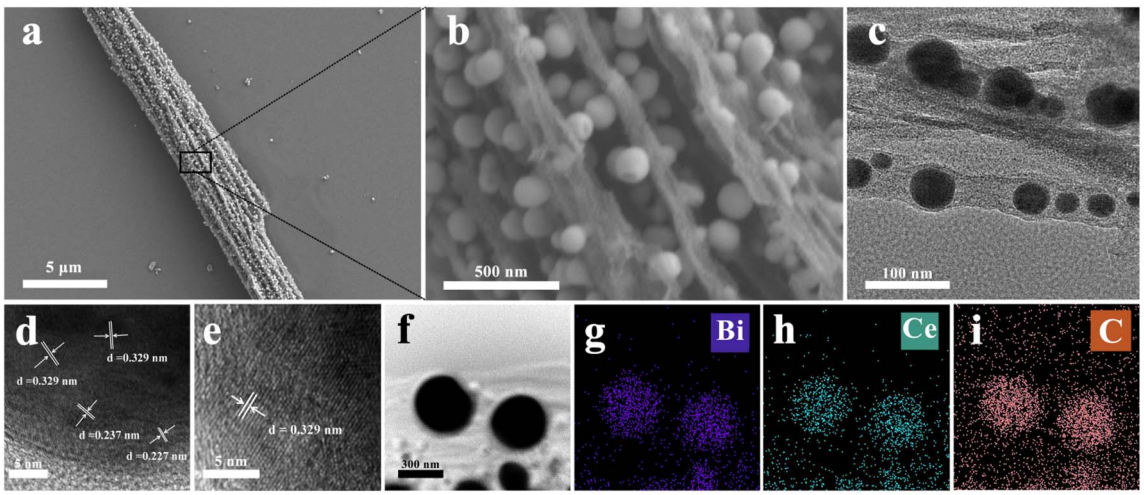

Fig. 1 Microstructure characterization of Ce_2–Bi@C. (a) SEM image. (b) Localized magnified image of (a). (c) TEM image. (d and e) HRTEM images. (f–i) EDS mappings.

 This journal is © The Royal Society of Chemistry 2024

Published on 06 mars 2024. Downloaded on 2.6.2026 13:51:06.

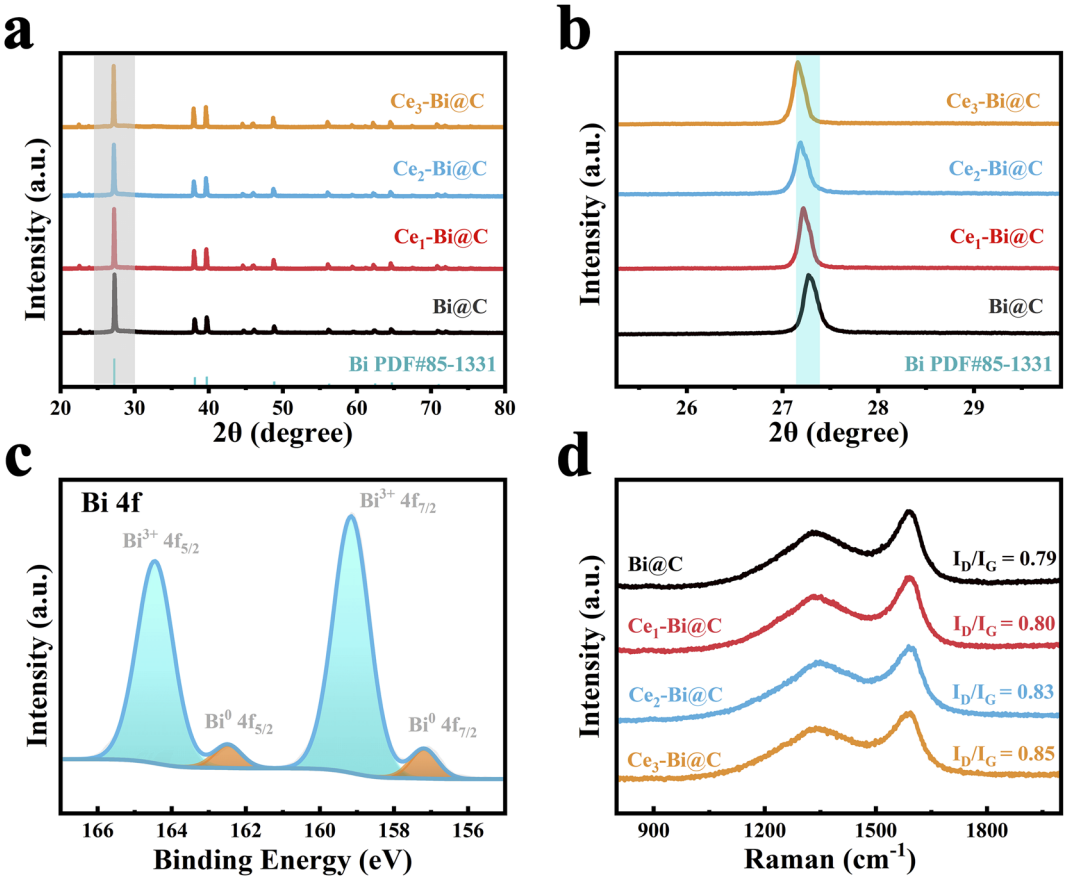

Fig. 2 (a) XRD patterns and (b) enlarged XRD patterns of Bi@C, Ce_1–Bi@C, Ce_2–Bi@C and Ce_3–Bi@C. (c) Bi 4f XPS spectra of Ce_2–Bi@C. (d) Raman spectra of various Bi-based composites.

has been successfully doped into Bi. In Fig. 2c and S9,† the high-resolution Bi 4f spectra can be deconvoluted into two distinct chemical states of Bi(0) species and Bi(III) species. In fact, it is a general phenomenon that Bi(III) species is present on the catalyst surface, as a result of the unavoidable oxidation of Bi in air.[31,32,34] In Fig. S10,† the high-resolution Ce 3d spectra indicate that the majority of the Ce present in Ce–Bi@C catalysts is in the Ce^{4+} oxidation state. Surface oxidation poses a challenge in obtaining the electron shift *via* XPS analysis. Additionally, the Raman spectrum exhibited two prominent peaks at 1328 and 1594 cm^{-1}, corresponding to the defect (D) and graphitic (G) carbon, respectively (Fig. 2d). It is worth noting that the I_D/I_G ratio gradually increases as the Ce content increases, resulting in the formation of defects in the carbon matrix after the introduction of Ce atoms. Based on the above discussion, the higher degree of graphitization in Bi@C is likely due to the increased precipitation of graphite carbon around the undoped Bi nanoparticles. Indeed, the D peak intensities are generally low, suggesting the high degree of graphitization for all catalysts. The high degree of carbon graphitization can enhance electron transfer during electrocatalysis.[49] In Fig. S11,† the specific surface area of Ce_2–Bi@C nanoparticles is 86.3 $m^2\ g^{-1}$, and there are abundant mesopores of approximately 3 nm, 4–20 nm and 25–50 nm on the carbon matrix. The wide size distribution of mesopores may be attributed to the interconnection of smaller pores, facilitating unimpeded mass transfer and exposing more Bi active sites, thereby effectively improving electrocatalytic performance.

The CO_2RR catalytic activities were evaluated in 0.1 M $KHCO_3$ aqueous electrolyte using a three-electrode H-cell (see the Experimental section in the ESI†). As shown in Fig. S12,† the linear scanning voltammetry (LSV) curves exhibit much higher cathodic current density in CO_2-saturated $KHCO_3$ solution for all Bi-based catalysts than those obtained in Ar-saturated electrolyte, indicating a greater preference for the CO_2RR over the hydrogen evolution reaction (HER). Besides, Ce_2–Bi@C has the highest current density and the lowest onset potential as shown in Fig. 3a, suggesting its superior CO_2RR activity compared with other Bi-based catalysts. The step-potential electrolysis was conducted at the applied potentials ranging from −0.8 to −1.3 V *vs.* RHE with on-line monitoring of the as-generated gas products,[50,51] while the liquid-phase products were quantified by 1H nuclear magnetic resonance (NMR) analysis using DMSO as an internal standard after electrolysis (Fig. S13†).[52] As illustrated in Fig. 3b, the electrolysis process only yielded three products: H_2, CO, and formate. For Ce_2–Bi@C, the faradaic efficiency (FE) for formate is consistently over 90% in a wide potential window from −0.9 to −1.3 V *vs.* RHE. Among them, FE($HCOO^-$) reaches

Published on 06 mars 2024. Downloaded on 2.6.2026 13:51:06.

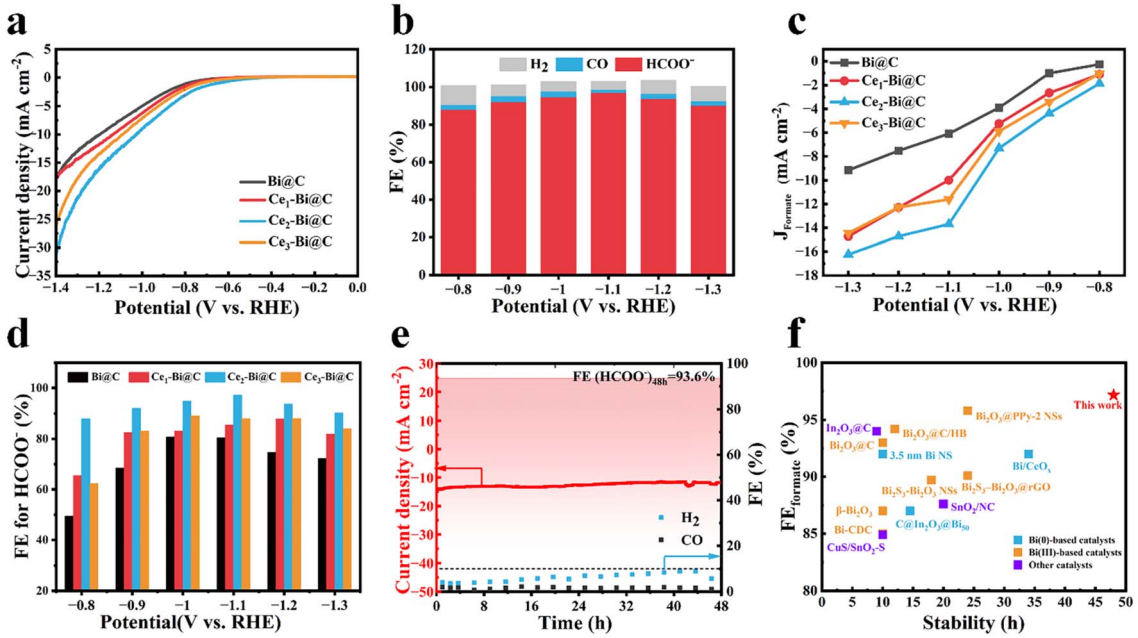

Fig. 3 Electrochemical measurements. (a) LSV curves of Bi@C, Ce_1–Bi@C, Ce_2–Bi@C and Ce_3–Bi@C in CO_2-saturated 0.1 M $KHCO_3$. (b) Faradaic efficiencies of the reduction products generated by Ce_2–Bi@C in 0.1 M CO_2-saturated $KHCO_3$ aqueous solution at different applied potentials. (c) $HCOO^-$ partial current densities and (d) potential-dependent FEs of $HCOO^-$ for Bi@C, Ce_1–Bi@C, Ce_2–Bi@C and Ce_3–Bi@C. (e) Amperometric *i*–*t* stability of Ce_2–Bi@C in 0.1 M $KHCO_3$ at −1.1 V *vs.* RHE. (f) Comparison of $FE_{formate}$ and stability for Ce_2–Bi@C and some recently reported catalysts for the CO_2RR.

an impressive 97.2% at −1.1 V *vs.* RHE. In Fig. S14,† the Tafel plot of Ce_2–Bi@C exhibits a slope of 150.1 mV dec^{-1} based on the method of linear fitting, which is higher than 118 mV dec^{-1}. Such a high Tafel slope indicates that the initial single-electron transfer of CO_2^- formation is the rate-determining step for Ce_2–Bi@C during the CO_2RR process of CO_2-to-formate conversion.[32,53]

The CO_2RR performances of other Bi-based catalysts were also evaluated as reference samples in Fig. S15–S21.† For comparison, the partial current densities and FEs for the $HCOO^-$ product were re-analyzed and are presented in Fig. 3c and d, respectively. The Bi@C catalyst exhibits an inferior activity with a maximum FE($HCOO^-$) of 80.8% at −1.0 V *vs.* RHE. After doping Ce into Bi@C, both the yield and FE for generating $HCOO^-$ gradually increased with the Ce content. Notably, Ce_2–Bi@C exhibits the best CO_2RR performance among all obtained catalysts, with a partial current density of 13.7 mA cm^{-2} and selectivity of 97.2% toward the formate product at −1.1 V *vs.* RHE. Surprisingly, the CO_2RR performance decreases withae further increase in Ce content. Clearly, Ce_2–Bi@C has the appropriate content of Ce doping for boosting CO_2RR performance. In Fig. S19,† the Ce-doped Bi@C samples exhibit a smaller charge-transfer resistance (R_{ct}) compared with the undoped Bi@C, with Ce_2–Bi@C showing the smallest R_{ct}. This suggests that the introduction of Ce dopants can accelerate the reaction kinetics for the CO_2RR at solid/solution interfaces. Thus, it can be safely inferred that the electronic structure of Bi sites is modulated by the Ce heteroatoms, contributing to the enhancement in adsorbing *OCHO intermediates and thereby the improvement in CO_2RR performance. In Fig. S20 and S21,† the electrochemical surface area (ECSA) of these catalysts is calculated using the double-layer capacitance method, indicating the generation of more active sites by doping Ce into Bi. In Fig. 3e, Ce_2–Bi@C exhibits a stable current density and maintains a high average FE($HCOO^-$) of 93.6% during 48 hour electrolysis. After the stability test, Fig. S22† shows that there is no obvious change in the microstructure, the Ce–Bi nanoparticles are not aggregated or damaged, no obvious difference is seen in the XRD results (Fig. S23†), and the XPS results indicate that there is no obvious change in the valence states of Bi and Ce (Fig. S24†), which are the results that further confirm the high stability of Ce_2–Bi@C. Such excellent stability can be attributed to the stable metallic Bi(0) and external carbon framework confinement during the CO_2RR process at the reduction potential. In Fig. 3f, our reported Ce_2–Bi@C CO_2RR catalyst demonstrates superior selectivity of formate and long-term durability obtained by using flooded half-cells compared with the majority of Bi-based catalysts reported in recent years.[17,19,22,24,25,30,31,53–58]

Finally, *in situ* attenuated total reflectance infrared (ATR-IR) spectroscopy and density functional theory (DFT) calculations were conducted to explore the possible reaction pathway and further elucidate the origin of observed improvement in CO_2RR performance for the Ce_2–Bi@C catalyst. Fig. 4a shows significantly enhanced peaks at 1374 $cm^{-1}$and 1419 cm^{-1} corresponding to bicarbonate (HCO_3^-).[59,60] Notably, at applied potentials higher than −0.4 V *vs.* RHE, a prominent peak appears at approximately 1395 cm^{-1}, which can be attributed to

 This journal is © The Royal Society of Chemistry 2024

Published on 06 mars 2024. Downloaded on 2.6.2026 13:51:06.

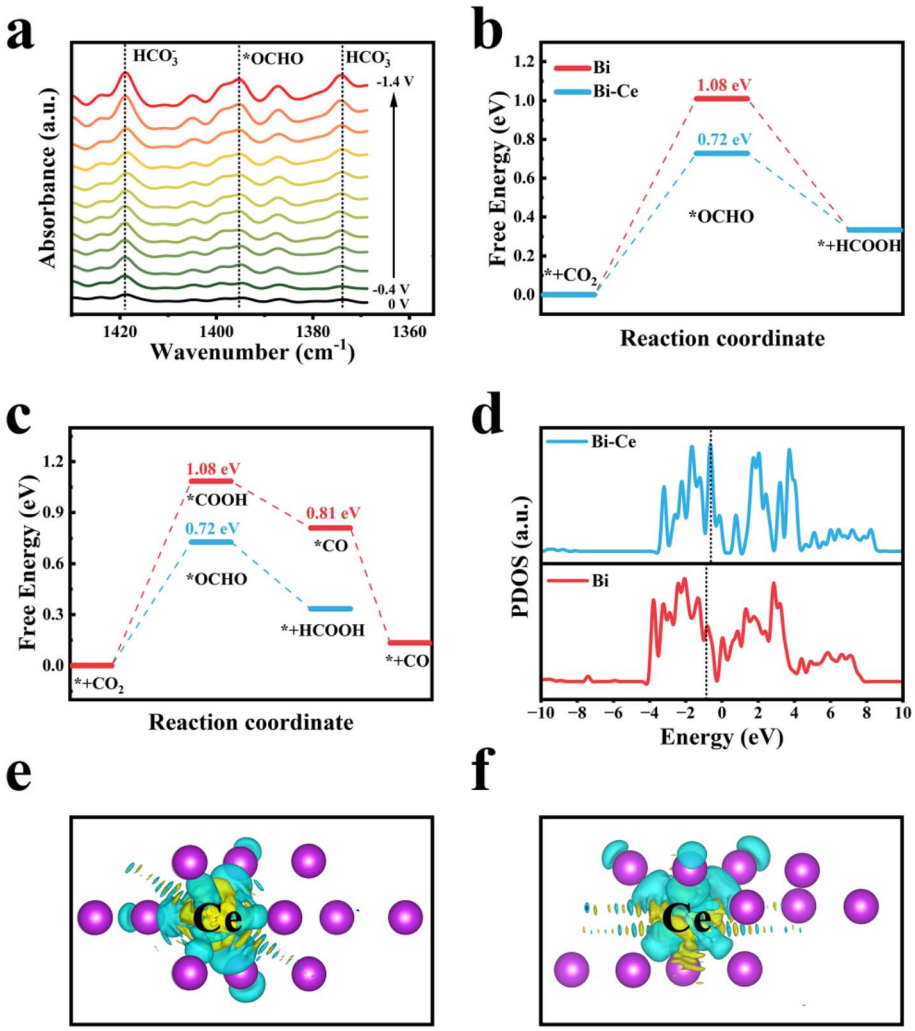

Fig. 4 (a) *In situ* ATR-IR spectra during electrochemical CO_2 reduction of the Ce_2–Bi@C electrocatalyst in a potential window from −0.4 V to −1.4 V *vs.* RHE. (b) Free energy diagrams for the CO_2 reduction reaction on Bi and the Ce–Bi surface. (c) Gibbs free energy diagrams for HCOOH and CO on the surface of Ce–Bi. (d) Projected density of states of p orbitals of Bi reaction sites of Bi and Ce–Bi. (e) Top and (f) side view of charge density difference maps, and cyan and yellow indicate the electron accumulation and depletion, respectively.

the vibration of the two oxygen-bridged bond (O–C–O) for formyloxyl radicals (*OCHO).[60,61] Furthermore, the intensity of this peak gradually increases with the higher potential, consistent with the increasing trend of formate evolution. Therefore, it can be inferred that *OCHO serves as the crucial intermediate in the CO_2RR process for formate formation. To demonstrate that the CO_2RR process takes place on the Ce-doped Bi nanoparticle surface, the metal poisoning experiment shows a marked reduction in current subsequent to the introduction of SCN^- as shown in Fig. S25.† These experimental observations suggest that the porous carbon framework does not completely cover the Ce–Bi nanoparticles (Fig. S6†), resulting in a negligible impedance of mass transfer. This result aligns with the DFT analysis depicted in Fig. S26.† Based on these results, catalyst models were constructed consisting of three layers of Bi(111) crystal facets. In the material under investigation, the atomic ratio of bismuth to cerium was precisely determined to be 16 : 1, a ratio selected based on our preliminary experimental optimization results. One Bi atom in the surface layer was substituted with Ce dopants to model the Ce_2–Bi structure. For CO_2 reduction to HCOOH, the mechanism involved two proton-coupled electron transfer (PCET) steps *via* *OCHO and *HCOOH. As depicted in Fig. 4b, the formation of *OCHO was the rate-determining step (RDS) for both Bi and Ce-doped Bi systems. The introduction of the Ce dopant greatly lowers the energy barrier of the RDS from 1.08 eV to 0.72 eV, consistent with a decreased overpotential of 110 mV. As shown in Fig. 4c and S29,† *OCHO exhibits a pronounced preference over *COOH for the first PCET step of CO_2 reduction, thereby favoring the pathway towards HCOOH rather than CO.[62] To further elucidate the effect of Ce doping, density of states (DOS) was analyzed, as shown in Fig. 4d. Upon introducing Ce into Bi, the center of the Bi p-band shifted towards the Fermi level from 1.176 eV to 0.485 eV, indicating an increased abundance of electron density in the Bi p-orbitals.[63–66] According to Bader charge analysis, the atomic charge of Ce is +1.2 $|e|$, also

Published on 06 mars 2024. Downloaded on 2.6.2026 13:51:06.

indicating electron transfer from the Ce dopant to the neighboring Bi.[67] The charge density difference in Fig. 4e and f clearly show the electron accumulation on the Bi atoms. The additional electron may enhance CO_2 adsorption on the catalyst's surface and promote the reduction process. These theoretical findings, combined with the *in situ* ATR-IR results, demonstrate that the significant improvement in CO_2RR performance of the Ce-doped Bi catalyst can be attributed to the modulation of the electronic structure that facilitates the adsorption of crucial *OCHO intermediates. A previous study also indicated that the Bi surface promotes CO_2 reduction to HCOOH rather than CO.[68] The alignment of our findings with prior studies lends credence to the proposed mechanism, whereby the modulation of the electronic structure in the Ce-doped Bi catalyst enhances the adsorption of the pivotal *OCHO intermediates, thereby improving CO_2RR performance.

In this study, an efficient catalyst of Ce-doped Bi encapsulated in a porous carbon framework was successfully synthesized *via* direct annealing of a MOF-based precursor under an inert gas atmosphere. We showed a significant improvement in CO_2RR performance for production of formate for a metallic Bi catalyst after Ce doping. Compared with conventional Bi(III)-based catalysts, the Bi(0)-based catalyst demonstrates an enhanced stability for the CO_2RR due to the highly stable structure of the metal during cathodic reduction. DFT calculations revealed that Ce doping increased the electron density around Bi, thereby strengthening the binding energy of crucial *OCHO intermediates, consequently enhancing the catalyst's activity towards formic acid. This work offers valuable insights for future research on catalyst design, particularly in terms of modulating electronic structures to enhance catalytic activity.

Author contributions

J. S. and Y. Z. conceived the idea and designed the experiments. Y. Z. and N. J. conducted material synthesis, the characterization studies of the materials, and the electrochemical test. Q. L. and L. W. contributed to the characterization of the electrocatalysts. S. L. conducted the DFT calculations and wrote the corresponding chapters. Z. T. and J. L. provided guidance on the DFT calculations. Y. Z. processed the experimental data and wrote the manuscript. J. S. revised and finalized the manuscript. J. S., Q. C. and Z. T. supervised the project. All authors discussed the results and commented on the manuscript.

Conflicts of interest

There are no conflicts of interest to declare.

Acknowledgements

This work was supported by the National Natural Science Foundation of China (No. 52002378 and 52171022), Anhui Provincial Natural Science Foundation (No. 2208085Y16), Zhejiang Provincial Natural Science Foundation of China (No. LXR22B030001), Excellent Research and Innovation Team Project of Anhui Province (2023AH010001), Ningbo Natural Science Foundation (No. 2021J198), "From 0 to 1" Innovative Program of CAS (No. ZDBS-LY-JSC021) and Open Project of Key Laboratory of Advanced Fuel Cells and Electrolyzers Technology of Zhejiang Province. The calculations were completed on the supercomputing system in the Supercomputing Center of NIMTE.

Notes and references

1 H. Xu, S. Ci, Y. Ding, G. Wang and Z. Wen, *J. Mater. Chem. A*, 2019, **7**, 8006–8029.
2 Z. Sun, T. Ma, H. Tao, Q. Fan and B. Han, *Chem*, 2017, **3**, 560–587.
3 Q. H. Low, N. W. X. Loo, F. Calle-Vallejo and B. S. Yeo, *Angew. Chem., Int. Ed.*, 2019, **58**, 2256–2260.
4 H. Yang, Y. Wu, G. Li, Q. Lin, Q. Hu, Q. Zhang, J. Liu and C. He, *J. Am. Chem. Soc.*, 2019, **141**, 12717–12723.
5 L. Xiong, X. Zhang, L. Chen, Z. Deng, S. Han, Y. Chen, J. Zhong, H. Sun, Y. Lian, B. Yang, X. Yuan, H. Yu, Y. Liu, X. Yang, J. Guo, M. H. Rümmeli, Y. Jiao and Y. Peng, *Adv. Mater.*, 2021, **33**, 2101741.
6 J. Qu, X. Cao, L. Gao, J. Li, L. Li, Y. Xie, Y. Zhao, J. Zhang, M. Wu and H. Liu, *Nano-Micro Lett.*, 2023, **15**, 178.
7 S. Grimme, J. Antony, S. Ehrlich and H. Krieg, *APL Mater.*, 2010, **132**, 154104.
8 M. Grasemann and G. Laurenczy, *Energy Environ. Sci.*, 2012, **5**, 8171–8181.
9 A. Vasileff, C. C. Xu, Y. Jiao, Y. Zheng and S. Z. Qiao, *Chem*, 2018, **4**, 1809–1831.
10 B. A. Rosen, A. Salehi-Khojin, M. R. Thorson, W. Zhu, D. T. Whipple, P. J. A. Kenis and R. I. Masel, *Science*, 2011, **334**, 643–644.
11 S. Gao, Y. Lin, X. C. Jiao, Y. F. Sun, Q. Q. Luo, W. H. Zhang, D. Q. Li, J. L. Yang and Y. Xie, *Nature*, 2016, **529**, 68.
12 C. Costentin, S. Drouet, M. Robert and J. M. Savéant, *Science*, 2012, **338**, 90–94.
13 W. Yang, S. Chen, W. Ren, Y. Zhao, X. Chen, C. Jia, J. Liu and C. Zhao, *J. Mater. Chem. A*, 2019, **7**, 15907–15912.
14 N. Zouaoui, B. D. Ossonon, M. Y. Fan, D. Mayilukila, S. Garbarino, G. de Silveira, G. A. Botton, D. Guay and A. C. Tavares, *J. Mater. Chem. A*, 2019, **7**, 11272–11281.
15 Z. B. Hoffman, T. S. Gray, K. B. Moraveck, T. B. Gunnoe and G. Zangari, *ACS Catal.*, 2017, **7**, 5381–5390.
16 L. Ma, N. Liu, B. Mei, K. Yang, B. Liu, K. Deng, Y. Zhang, H. Feng, D. Liu and J. Duan, *ACS Catal.*, 2022, **12**, 8601–8609.
17 Z. T. Wang, Y. S. Zhou, D. Y. Liu, R. J. Qi, C. F. Xia, M. T. Li, B. You and B. Y. Xia, *Angew. Chem., Int. Ed.*, 2022, **61**, e202200552.
18 L. Shang, X. Lv, L. Zhong, S. Li and G. Zheng, *Small Methods*, 2022, **6**, 2101334.
19 Z. Wu, H. Jing, Y. Zhao, K. Lu, B. Liu, J. Yu, X. Xia, W. Lei and Q. Hao, *Chem. Eng. J.*, 2023, **451**, 138477.
20 X. Zhang, Y. Zhang, Q. Li, X. Zhou, Q. Li, J. Yi, Y. Liu and J. Zhang, *J. Mater. Chem. A*, 2020, **8**, 9776–9787.
21 S. Frank, E. Svensson Grape, E. D. Bøjesen, R. Larsen, P. Lamagni, J. Catalano, A. K. Inge and N. Lock, *J. Mater. Chem. A*, 2021, **9**, 26298–26310.

 This journal is © The Royal Society of Chemistry 2024

Published on 06 mars 2024. Downloaded on 2.6.2026 13:51:06.

22 X. Yang, P. Deng, D. Liu, S. Zhao, D. Li, H. Wu, Y. Ma, B. Y. Xia, M. Li, C. Xiao and S. Ding, *J. Mater. Chem. A*, 2019, **8**, 2472–2480.
23 D. Wu, G. Huo, W. Chen, X.-Z. Fu and J.-L. Luo, *Appl. Catal., B*, 2020, **271**, 118957.
24 S.-Q. Liu, E. Shahini, M.-R. Gao, L. Gong, P.-F. Sui, T. Tang, H. Zeng and J.-L. Luo, *ACS Nano*, 2021, **15**, 17757–17768.
25 X. Hu, J. Sun, W. Zheng, S. Zheng, Y. Xie, X. Gao, B. Yang, Z. Li, L. Lei and Y. Hou, *Chin. J. Chem. Eng.*, 2022, **43**, 116–123.
26 Y. Yuan, Q. Wang, Y. Qiao, X. Chen, Z. Yang, W. Lai, T. Chen, G. Zhang, H. Duan and M. Liu, *Adv. Energy Mater.*, 2022, **12**, 2200970.
27 S. Yang, M. Jiang, W. Zhang, Y. Hu, J. Liang, Y. Wang, Z. Tie and Z. Jin, *Adv. Funct. Mater.*, 2023, **33**, 2301984.
28 J. Lee, H. Liu, Y. Chen and W. Li, *ACS Appl. Mater. Interfaces*, 2022, **14**, 14210–14217.
29 Y. Huang, A. G. A. Mohamed, J. Xie and Y. Wang, *Nano Energy*, 2021, **82**, 105745.
30 D. Yao, C. Tang, A. Vasileff, X. Zhi, Y. Jiao and S. Z. Qiao, *Angew. Chem., Int. Ed.*, 2021, **60**, 18178–18184.
31 P. Deng, F. Yang, Z. Wang, S. Chen, Y. Zhou, S. Zaman and B. Y. Xia, *Angew. Chem., Int. Ed.*, 2020, **59**, 10807–10813.
32 S. Liu, Y. Fan, Y. Wang, S. Jin, M. Hou, W. Zeng, K. Li, T. Jiang, L. Qin, Z. Yan, Z. Tao, X. Zheng, C. Shen, Z. Liu, T. Ahmad, K. Zhang and W. Chen, *Nano Lett.*, 2022, **22**, 9107–9114.
33 Q. Wang, X. Yang, H. Zang, C. Liu, J. Wang, N. Yu, L. Kuai, Q. Qin and B. Geng, *Small*, 2023, **19**, 2303172.
34 B. Ren, G. Wen, R. Gao, D. Luo, Z. Zhang, W. Qiu, Q. Ma, X. Wang, Y. Cui and L. Ricardez-Sandoval, *Nat. Commun.*, 2022, **13**, 2486.
35 J. Su, R. Ge, K. Jiang, Y. Dong, F. Hao, Z. Tian, G. Chen and L. Chen, *Adv. Mater.*, 2018, **30**, 1801351.
36 H. Huang, S. Chen, P. Jiang, Y. Yang, C. L. Wang, W. Zheng, Z. Y. Cheng, M. X. Huang, L. Hu and Q. W. Chen, *Adv. Funct. Mater.*, 2023, **33**, 2300475.
37 X. Li, X. Q. Wu, J. J. Li, J. B. Huang, L. Ji, Z. H. Leng, N. K. Qian, D. R. Yang and H. Zhang, *Nanoscale*, 2021, **13**, 19610–19616.
38 G. X. Zhang, X. L. Zheng, X. M. Cui, J. Wang, J. H. Liu, J. F. Chen and Q. Xu, *ACS Appl. Nano Mater.*, 2022, **5**, 15465–15472.
39 Z. C. Zeng, Y. S. Xu, Z. S. Zhang, Z. S. Gao, M. Luo, Z. Y. Yin, C. Zhang, J. Xu, B. L. Huang, F. Luo, Y. P. Du and C. H. Yan, *Chem. Soc. Rev.*, 2020, **49**, 1109–1143.
40 S. Zhang, S. E. Saji, Z. Yin, H. Zhang, Y. Du and C. H. Yan, *Adv. Mater.*, 2021, **33**, 2005988.
41 N. Zhang, Y. Yi, J. Lian and Z. Fang, *Chem. Eng. J.*, 2020, **395**, 124897.
42 J. Bai, R.-T. Gao, X. Guo, J. He, X. Liu, X. Zhang and L. Wang, *Chem. Eng. J.*, 2022, **448**, 137602.
43 J. Su, Y. Yang, G. Xia, J. Chen, P. Jiang and Q. Chen, *Nat. Commun.*, 2017, **8**, 14969.
44 A. Reina, X. T. Jia, J. Ho, D. Nezich, H. B. Son, V. Bulovic, M. S. Dresselhaus and J. Kong, *Nano Lett.*, 2008, **9**, 30–35.
45 A. G. Sokol, A. F. Khokhryakov, Y. M. Borzdov, I. N. Kupriyanov and Y. N. Palyanov, *Am. Mineral.*, 2019, **104**, 1857–1865.
46 H. Z. Liu, X. Liu, B. Li, H. Q. Luo, J. G. Ma and P. Cheng, *ACS Appl. Mater. Interfaces*, 2022, **14**, 28123–28132.
47 X. Y. Wang, Y. X. Wang, B. Robinson, Q. Wang and J. L. Hu, *J. Catal.*, 2022, **413**, 138–149.
48 C. W. Lee, J. S. Hong, K. D. Yang, K. Jin, J. H. Lee, H.-Y. Ahn, H. Seo, N.-E. Sung and K. T. Nam, *ACS Catal.*, 2018, **8**, 931–937.
49 Y. Y. Guan, X. R. Zhang, Y. X. Zhang, T. N. V. Karsili, M. Y. Fan, Y. Y. Liu, B. Marchetti and X. D. Zhou, *J. Colloid Interface Sci.*, 2022, **612**, 235–245.
50 J. Su, D. Pan, Y. Dong, Y. Zhang, Y. Tang, J. Sun, L. Zhang, Z. Tian and L. Chen, *Adv. Energy Mater.*, 2023, 2204391.
51 Y. Dong, Q. Zhang, Z. Tian, B. Li, W. Yan, S. Wang, K. Jiang, J. Su, C. W. Oloman and E. L. Gyenge, *Adv. Mater.*, 2020, **32**, 2001300.
52 A. Xu, X. Chen, D. Wei, B. Chu, M. Yu, X. Yin and J. Xu, *Small*, 2023, **19**, 2302253.
53 Y. X. Duan, Y. T. Zhou, Z. Yu, D. X. Liu, Z. Wen, J. M. Yan and Q. Jiang, *Angew. Chem., Int. Ed.*, 2021, **60**, 8798–8802.
54 T. Tran-Phu, R. Daiyan, Z. Fusco, Z. Ma, R. Amal and A. Tricoli, *Adv. Funct. Mater.*, 2020, **30**, 1906478.
55 Y. Xu, Y. Guo, Y. Sheng, H. Yu, K. Deng, Z. Wang, X. Li, H. Wang and L. Wang, *Small*, 2023, **19**, 2300001.
56 P. F. Sui, C. Xu, M. N. Zhu, S. Liu, Q. Liu and J. L. Luo, *Small*, 2022, **18**, 2105682.
57 J. Zhai, Y. Hu, M. Su, J. Shi, H. Li, Y. Qin, F. Gao and Q. Lu, *Small*, 2023, **19**, e2206440.
58 T. Dou, J. He, S. Diao, Y. Wang, X. Zhao, F. Zhang and X. Lei, *J. Energy Chem.*, 2023, **82**, 497–506.
59 Q. Zhang, M. Sun, C.-Y. Yuan, Q.-W. Sun, B. Huang, H. Dong and Y.-W. Zhang, *ACS Catal.*, 2023, **13**, 7055–7066.
60 Z. Chen, D. Zhang, Q. Li, H. Zhang, Y. Zhao, Q. Ke, Y. Yan, L. Liu, M. Liu and X. He, *Appl. Catal., B*, 2024, **341**, 123342.
61 Y. Li, J. Chen, S. Chen, X. Liao, T. Zhao, F. Cheng and H. Wang, *ACS Energy Lett.*, 2022, **7**, 1454–1461.
62 Y. Tuo, Q. Lu, W. Liu, M. Wang, Y. Zhou, X. Feng, M. Wu, D. Chen and J. Zhang, *Small*, 2021, **17**, 2306945.
63 J. K. Nørskov, F. Abild-Pedersen, F. Studt and T. Bligaard, *Proc. Natl. Acad. Sci. U.S.A.*, 2011, **108**, 937–943.
64 A. Nilsson, L. Pettersson, B. Hammer, T. Bligaard, C. H. Christensen and J. K. Nørskov, *Catal. Lett.*, 2005, **100**, 111–114.
65 W. Zhang, L. Wang, H. Liu, Y. Hao, H. Li, M. U. Khan and J. Zeng, *Nano Lett.*, 2017, **17**, 788–793.
66 B. Hammer and J. K. Nørskov, in *Advances in Catalysis*, Elsevier, 2000, vol. 45, pp. 71–129.
67 W. Tang, E. Sanville and G. Henkelman, *J. Phys.: Condens.Matter*, 2009, **21**, 084204.
68 Y. Wang, T. Liu and Y. Li, *Chem. Sci.*, 2022, **13**, 6366–6372.